SCIENCE CHINA
Information Sciences

• RESEARCH PAPER •

December 2024, Vol. 67, Iss. 12, 222402:1–222402:11
https://doi.org/10.1007/s11432-024-4191-5

Physical origin of planar linear dichroism in van der Waals semiconductors using main group elements

Qiang GAO[1,2], Yali YU[1,3], Kaiyao XIN[1,3], Ziqi ZHOU[1], Hui-Xiong DENG[1,3], Lin LI[4,5], Xiaojie TANG[4], Congxin XIA[4], Duan-Yang LIU[1], Jian-Bai XIA[1,3], Jun KANG[2*] & Zhongming WEI[1,3*]

[1]*State Key Laboratory of Superlattices and Microstructures, Institute of Semiconductors, Chinese Academy of Sciences, Beijing* 100083*, China;*
[2]*Beijing Computational Science Research Center, Beijing* 100193*, China;*
[3]*Center of Materials Science and Optoelectronics Engineering, University of Chinese Academy of Sciences, Beijing* 100049*, China;*
[4]*School of Physics, Henan Key Laboratory of Photovoltaic Materials, Henan Normal University, Xinxiang* 453007*, China;*
[5]*School of Physics and Optoelectronic Engineering, Zhengzhou Key Laboratory of Low-Dimensional Quantum Materials and Devices, Zhongyuan University of Technology, Zhengzhou* 450007*, China*

Received 11 July 2024/Revised 1 August 2024/Accepted 14 October 2024/Published online 20 November 2024

Abstract The polarization of light can provide abundant information regarding the polarization degree, phase shift, and Jones vector, which is important in light communication, environmental scanning, quality inspection, etc. Recently, two-dimensional (2D) semiconductors have provided an ideal platform for detecting polarized light due to their remarkable and tunable linear dichroism (LD). However, the physical mechanism of the in-plane LD in 2D semiconductors has not been systematically investigated, limiting the further exploration of the 2D anisotropic semiconductors and the directionality of experiments on polarization photodetection. In this study, the in-plane LD of 100 types of 2D semiconductors composed of main group elements is investigated via first-principles theory combined with the decision tree algorithm and experimental measurement. The in-plane asymmetry of the lattice and band edge wavefunctions are the main origins of the in-plane LD. 2D semiconductors with in-plane orthorhombic and monoclinic lattices tend to have considerable in-plane LD, while their hexagonal counterparts are optically isotropic. Specifically, orthorhombic 2D semiconductors possess larger in-plane LD because their intrinsic mirror planes in the lattice induce in-plane parity of the wavefunctions at the band edges. The decision tree algorithm further reveals that in-plane LD is also related to the difference for the a and b lattice constants and the electronegativity difference between the cation and anion. In addition, heterostructures formed from these 2D semiconductors exhibit high light absorption, strong in-plane LD, and various types of band alignment. The result of our study can promote the application and development of 2D semiconductors in polarization optoelectronics.

Keywords 2D semiconductor, linear dichroism, optical properties, in-plane symmetry, main group elements

1 Introduction

Linear dichroism (LD) is a form of electromagnetic spectroscopy that refers to the difference in the optical absorption of polarized light with a polarization direction parallel (perpendicular) to a given orientation of a crystal [1–7]. Recently, the use of LD in materials has provided new opportunities for many modern photonic and optoelectronic devices and applications [8–15]. For example, by utilizing polarizer arrays or anisotropic materials, polarization-sensitive photodetection can be attained and provide rich information about an object, such as intensity, spectral, and polarization; this information can be applied to target tracking [16], remote sensing [17, 18], and computer vision [19]. Commercial polarization-sensitive photodetectors all rely on a polarizing lens array in front of the detection unit, which leads to a larger size and complicated configuration of the entire system. The increase in two-dimensional (2D) semiconductors with in-plane optical anisotropy provides a promising platform that can act as an intrinsic polarizer and

* Corresponding author (email: zmwei@semi.ac.cn, jkang@csrc.ac.cn)

a photosensitive unit at the same time; thus, the volume and configuration of the system are both simplified [20–30]. Some prototype 2D materials with significant optical anisotropy have been discovered; these materials include black phosphorene (BP), TiS_3, $ReSe_2$, GeSe, and $PdSe_2$ [31–36]. Further research on polarization optoelectronics needs to focus on developing more 2D semiconductors with strong in-plane LD and high stability, and the design principle should focus on 2D materials composed of group III, IV, V, and VI (main group) elements. The materials made of these main group elements exhibit intrinsically good optical and transport properties due to their strong *s*-*p* covalent bonding characteristics; this is also one of the reasons for their wide use in modern semiconductor technology [37–40]. However, systematic theoretical analysis of the in-plane LD of 2D semiconductors composed of these main group elements has not been performed. The investigation of the general trends that determine the optical anisotropy of materials is critical for the design of new 2D semiconductors with strong LD and the development of polarization-sensitive device applications.

Here, we constructed a comprehensive 2D anisotropic material database encompassing 100 different types of materials; these materials include binary compounds, elementary materials, and their van der Waals (vdW) heterostructures; additionally, we investigated their optical LD and examined their underlying physical mechanisms using first-principles calculations, employing density functional theory (DFT) with vdW correction. According to their in-plane symmetry, the studied 2D materials can be classified into three groups: orthorhombic, monoclinic, and hexagonal lattices. Compared with hexagonal lattices, crystals with orthorhombic and monoclinic lattices have a greater propensity for in-plane LDs. Notably, compounds with orthorhombic structure display larger LD values than those with a monoclinic structure, and their larger LD values are attributed to the presence of an intrinsic mirror plane within the lattice, resulting in the in-plane parity of the wavefunctions at the band edges. Moreover, calculations based on the decision tree algorithm further demonstrate that the in-plane LD is influenced by the difference for the a and b lattice constants and the electronegativity difference between cations and anions. Importantly, the heterostructures constructed from specific 2D semiconductors exhibit enhanced optical absorption and strong optical LD. Various types of band offsets (type-I, type-II, and type-III) exist among all considered 2D semiconductors; these semiconductors have the potential to facilitate the development of diverse functionalities and applications.

2 Methods

2.1 DFT calculation

All first-principles calculations were carried out based on the projector augmented wave (PAW) method as implemented in the Vienna ab initio simulation package (VASP) [41]. The exchange-correlation potential is described by the Perdew-Burke-Ernzerhof (PBE) functional of the generalized gradient approximation (GGA) [42]. To obtain an accurate band gap and optical property, the HSE06 function with a mixing parameter of 0.25 is used for band structure calculation [43]. The energy cutoff for the plane wave is set to 450 eV. The 2D crystal structures were built using the primitive cell, with a vacuum space of 20 Å to avoid the supercell image interaction. The crystal structures were relaxed using the PBE functional, considering the DFT-D3 method for the treatment of van der Waals interaction [44]. The convergence criteria of forces and energies are chosen to be 0.01 eV/Å and 10^{-5} eV for structure relaxation and self-consistence calculations. For the optical calculation, only the direct transition at the direct band edge is considered. The absorption coefficient is calculated using $\alpha(\omega) = \sqrt{2}\omega[\sqrt{\varepsilon_1^2(\omega) + \varepsilon_2^2(\omega)} - \varepsilon_1(\omega)]^{\frac{1}{2}}$ with $\varepsilon_1(\omega)$ and $\varepsilon_2(\omega)$ being the real part and imaginary part of the complex dielectric functions, respectively. The optical linear dichroism is calculated following the formula of LD $= a_x/a_y$, with a_x and a_y referring to absorption coefficients along x and y directions [6]. LD = 1 corresponds to optical isotropy, while LD > 1 or < 1 indicates optical anisotropy, and the anisotropy is stronger when the deviation of LD from 1 is larger. The optoelectronic-transport properties of 2D II-VI semiconductor-based photodetectors are simulated via nonequilibrium Green's function method within density functional theory programmed in the Quantum ATK 2021 package [45–47]. The basis set of norm-conserving Pseudo Dojo pseudopotentials is employed [47]. The K-point meshes and cut off are set to $1 \times 30 \times 150$ and 120 Hartree, respectively. The temperature is set to 300 K. The photocurrent is calculated using first-order perturbation theory

within the first Born approximation [48]. The photocurrent $I_{\rm ph}$ is calculated using the following formula:

$$I_{\rm ph} = \frac{e}{\hbar}\int \frac{{\rm d}E}{2\pi}\sum_{k,\alpha} T_\alpha(E,k), \tag{1}$$

where $T_\alpha(E,k)$ is the effective transmission coefficients and expressed by

$$T_\alpha(E,k) = {\rm Tr}\left\{i\Gamma_\alpha(E,k)\left[(1-f_\alpha)G^< + f_\alpha G^>\right]\right\} \tag{2}$$

with $G^{<(>)}$ denoting the noninteracting Green functions, and Γ_α and f_α denoting line width and Fermi distribution function of the α (left or right) electrode, respectively.

2.2 Devices fabrication and measurements

The nanosheets of GeSe, SnSe, SnS, and GeS were prepared by mechanical exfoliating from corresponding single crystals. Then they were transferred to a silicon wafer topped with a 300 nm SiO_2 layer. The electrode pattern was defined by using photolithography technology. Au was evaporated with a thickness of 50 nm through thermal evaporation. The optoelectronic measurements were conducted using an Agilent Technologies B1500A semiconductor device analyzer. With the assistance of a Glan-Taylor prism and a half-wave plate, the incident light polarized angle with respect to the crystal orientation can be adjusted to modulate the output polarization-sensitive current. The wavelength of incident light is 638 nm, and the power density of the incident light is 20 mW/cm^2.

3 Results and discussion

3.1 Classification of the prototypical 2D materials

The research protocol starts from the classification of all considered 2D materials in terms of their in-plane crystal symmetries, which can help to determine the general mapping principle between the lattice symmetry and the optical anisotropy. Figure 1(a) depicts the periodic table containing the elements (groups III, IV, V, and VI) for which we chose to construct 2D compounds and elementary materials. The considered 2D materials can be classified into three categories in view of their in-plane crystal symmetries: orthorhombic, monoclinic, and hexagonal. Here, the monoclinic 2D materials are defined as lattice vectors a that are not perpendicular to vector b, while both a and b are perpendicular to c. The orthorhombic 2D materials are defined as vectors $a \neq b \neq c$, where a, b, and c are perpendicular to each other. The hexagonal system is defined as $a = b$, and their intersection angle equals 120°. The corresponding space group of each structure is also provided (Figure S1). Note that compounds formed from heavy or toxic elements such as Tl, Pb, and Po are excluded due to their harmful effects on the environment. Figure 1(b) shows the top views of the crystal structures of 10 prototypical 2D semiconductors, covering all 3 categories of crystal structures.

3.2 2D optical LD database

By first-principles calculations, we obtained 100 2D structures to explore candidates with promising in-plane optical anisotropy, covering 10 elementary materials (such as tellurene, phosphorene, and arsenene), 65 binary compounds, and 25 vdW heterostructures [49]. For materials used with polarization-sensitive photodetection, the electronic structure and optical anisotropy are two critical factors that determine the absorption efficiency and linear dichroism, respectively. To visualize the electronic and optical properties and determine the general trends, we present the electronic bandgap and optical anisotropy of all considered 2D materials in Figure 2. Figure 2(a) shows that the bandgap of all considered 2D materials ranges from 0 to 5.29 eV, covering the infrared to ultraviolet spectrum. Among these 2D materials, there are approximately 10 wide bandgap (WBG) semiconductors (bandgap $\geqslant$ 3 eV) and 9 narrow bandgap semiconductors (bandgap $\leqslant$ 1 eV). To clearly determine the optoelectronic properties, we also calculated band structures using accurate hybrid functions, as shown in Figure S2. The band structure of the majority is indirect, although the bandgap difference between the direct and indirect cases for some materials is minimal. For example, the direct gap in GeSe is only slightly larger than its intrinsic indirect gap. The in-plane LD based on the minimal direct gap transition was calculated and is shown in Figure 2(b). Through

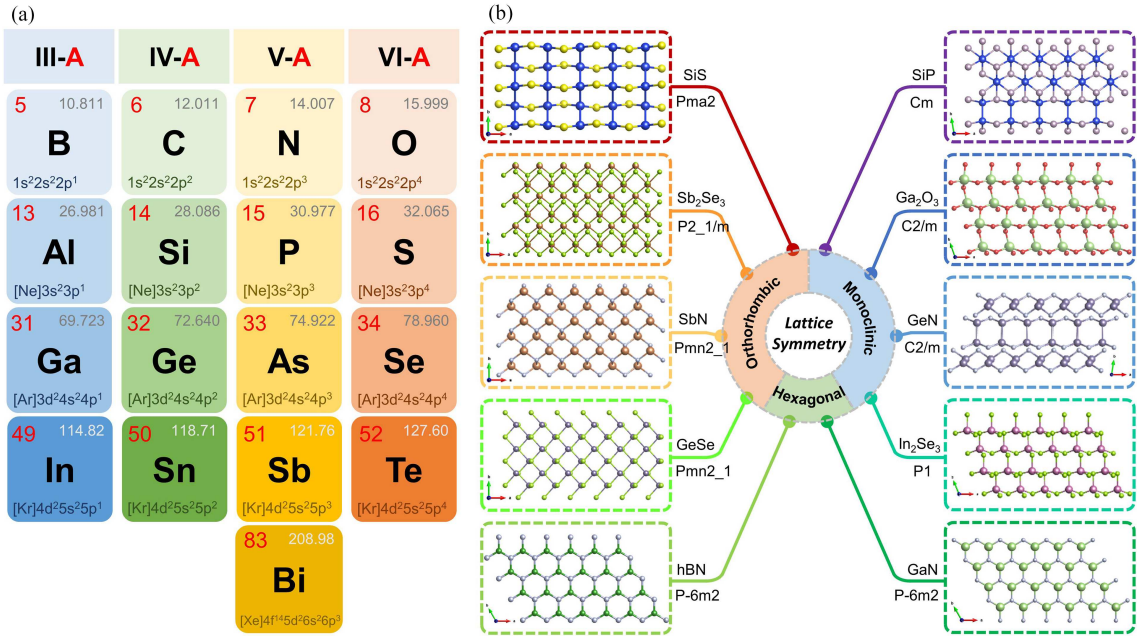

Figure 1 (Color online) (a) Groups III–VI elements considered to form 2D materials. C, Si, Ge, Sn, Sb, Bi, B, Al, and Ga form the cations, and O, S, Se, Te, N P, and As are selected to form the anions of the corresponding compounds. C, Si, Ge, Sn, Sb, Bi, and B can also form the elementary monolayers, such as graphene, silicene, and germanene. (b) Crystal structures of the ten prototypical 2D materials, such as monolayer Sb_2Se_3, SiS, and SbN, from three crystal systems—orthorhombic, monoclinic, and hexagonal—in view of their in-plane symmetry and dependence on the orientation of their lattice vectors.

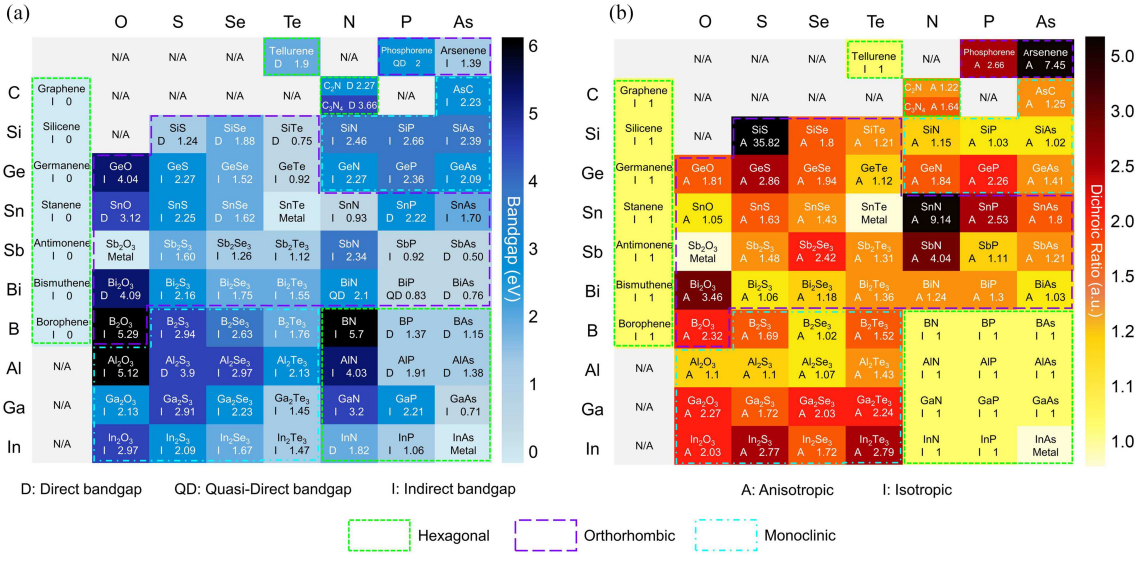

Figure 2 (Color online) (a) Map of the electronic bandgap of all considered 2D materials, including direct (D) quasi-direct (QD) and indirect (I) bandgaps. The number in each small box shows the bandgap of the corresponding material. (b) Map of the dichroic ratio of all considered 2D materials. The number in each small box represents the linear dichroic ratio, together with the corresponding color map. The three in-plane lattice types, hexagonal, orthorhombic, and monoclinic, are distinguished with different dashed-line boxes.

classification in terms of the in-plane lattice symmetry, a trend is observed; here, the optical anisotropy is strongly dependent on the in-plane symmetry of the crystal structures (crystal systems) rather than the specific space groups. Orthorhombic and monoclinic crystals are expected to possess optical anisotropy. In contrast, the compounds with orthorhombic structures show greater optical anisotropy than those with monoclinic structures. The highest linear dichroism ratio of 35.82 was observed for SiS, which has an orthorhombic structure in the IV-VI family. For polarized optoelectronic applications, bandgap and LD are the two key parameters that should be considered. SnN possesses a small bandgap (∼0.93 eV) and

strong linear dichroism (∼9.14) and can be applied to NIR polarization detectors. SnS, GeSe [50], SiS, and arsenene [51] can be used as building blocks for visible-light polarization photodetectors because of their suitable bandgap and strong LD. GeO and Bi_2O_3 show high potential in the field of UV polarization detection due to their large bandgaps (∼4.04 and 4.09 eV, respectively) and strong LD (∼1.81 and 3.46, respectively). For 2D elementary materials, only phosphorene and arsenene possess optical anisotropy with a nonzero bandgap due to their orthorhombic crystal structures and structural asymmetry along the *a*- and *b*-vector directions. Tellurene only possesses a direct bandgap (1.2 eV) without any optical anisotropy because of its symmetric hexagonal crystal structure, which is in good agreement with previous studies [52,53]. Notably, the lattice symmetries of all III-V compounds discussed here are hexagonal instead of a well-known sphalerite structure, resulting in the absence of optical anisotropy. Moreover, the hexagonal lattice is more stable for these 2D materials. The III-VI, IV-V, and IV-VI compounds have either orthorhombic or monoclinic structures, with significant optical anisotropy. Notably, some important III-VI 2D semiconductors not only exhibit orthorhombic symmetry but also exhibit hexagonal and monoclinic symmetry. Within the hexagonal phase, they are optically isotropic and thermodynamically stable. For example, 2D ultrathin GaS and GaSe layers have been successfully synthesized on SiO_2/Si substrates through the micromechanical cleavage method [54, 55], and GaTe nanosheets have been prepared through chemical vapor deposition [56]. Monoclinic GaX has a C2/m space group, showing optical anisotropy and a direct bandgap (GaTe). The results of quantitative analysis of the optical absorption coefficient and optical dichroic ratio (near band edges) of some prototypical 2D materials are shown in Figure 3. The absorption coefficient for these single materials is large (10^{-4} cm^{-1}), and the absorption spectra show a broad band (1.5–5 eV). A strong LD for the optical transition at the band edges is also observed. The strong optical anisotropy of 2D semiconductors is expected to show polarized-transport properties for related optoelectronic devices. Here, the optoelectronic-transport properties of related 2D semiconductor-based photodetectors were calculated, considering the effect of linearly polarized light. Figure 3(a) shows the side view of the two-probe model photodetector used for transport calculations. The transport system is formed of three parts, including left and right lead structures, and scattering region. The left and right electrodes are semi-infinite in length along the transport direction of armchair (zigzag). A small bias voltage of 0.5 V is exerted between the source and drain to generate a stable photocurrent along armchair (zigzag) orientation. Additionally, a polarized light with a wavelength of 638 nm is vertically applied to the system, and the angle θ in the *b*-*c* plane is defined as the polarization angle of incident light. The polarization-angle dependent photocurrent for GeSe (Figure 3(d)), GeS, SnS, SnSe, and SnS/GeSe vdW heterostructures-based (Figure S3) photodetectors was plotted in the polar coordinate system. It clearly shows the photocurrent is very sensitive to the polarization angle, and generates two-lobed polar plots. Moreover, the photocurrent along the zigzag orientation is larger than that along the armchair orientation, indicating strong transport anisotropy. Additionally, we consider the stacking effect on the optical properties through the formation of 2D vdW heterostructures. Due to certain optical anisotropy along the armchair and zigzag orientations for single materials, we constructed vdW heterostructures without any rotation angle. The calculated optical absorbance and linear dichroism are provided in Figure S4. Compared to that of monolayers, the optical absorption was clearly enhanced (Figure S4(a)). It could be attributed to the increase in the joint density of states and oscillator strength near the band edges. At the same time, the optical linear dichroism of the 2D vdW heterostructures is well preserved due to the structural asymmetry of each monolayer. Moreover, at the direct-gap minimum, strong polarization is also observed.

To further verify the first-principles prediction that materials with in-plane orthorhombic structures are expected to show strong optical anisotropy, related experiments were conducted. Photodetectors based on 2D IV-VI GeSe(S) and SnSe(S) materials were fabricated, and the polarization sensitivity and ambient stability were also tested because of the similar arrangement of atoms in the lattice for these four materials. Figure S5(a) shows a schematic diagram of the device. The electrodes were constructed along the armchair and zigzag of the materials using photolithography (the inset of Figure 3(e) and Figure S5). Figure 3(e) (Figure S6) shows orientation-dependent I-V curves of a typical GeSe- (GeS- and SnSe(S)-) based device measured under 638 nm laser illumination and dark conditions. The modulated laser beam was first set to pass through a polarizer and halfwave plate (HWP), and finally illuminated on the samples. The polarized photocurrent was measured by rotating the HWP every 15° to change the polarization direction, while keeping the incident power constant. We note that if the vibration plane of the linear polarized incident light makes an angle of θ to the main section of the HWP, the transmission light goes around the angle of 2θ from the original orientation. The photocurrent along the *a*-axis is greater

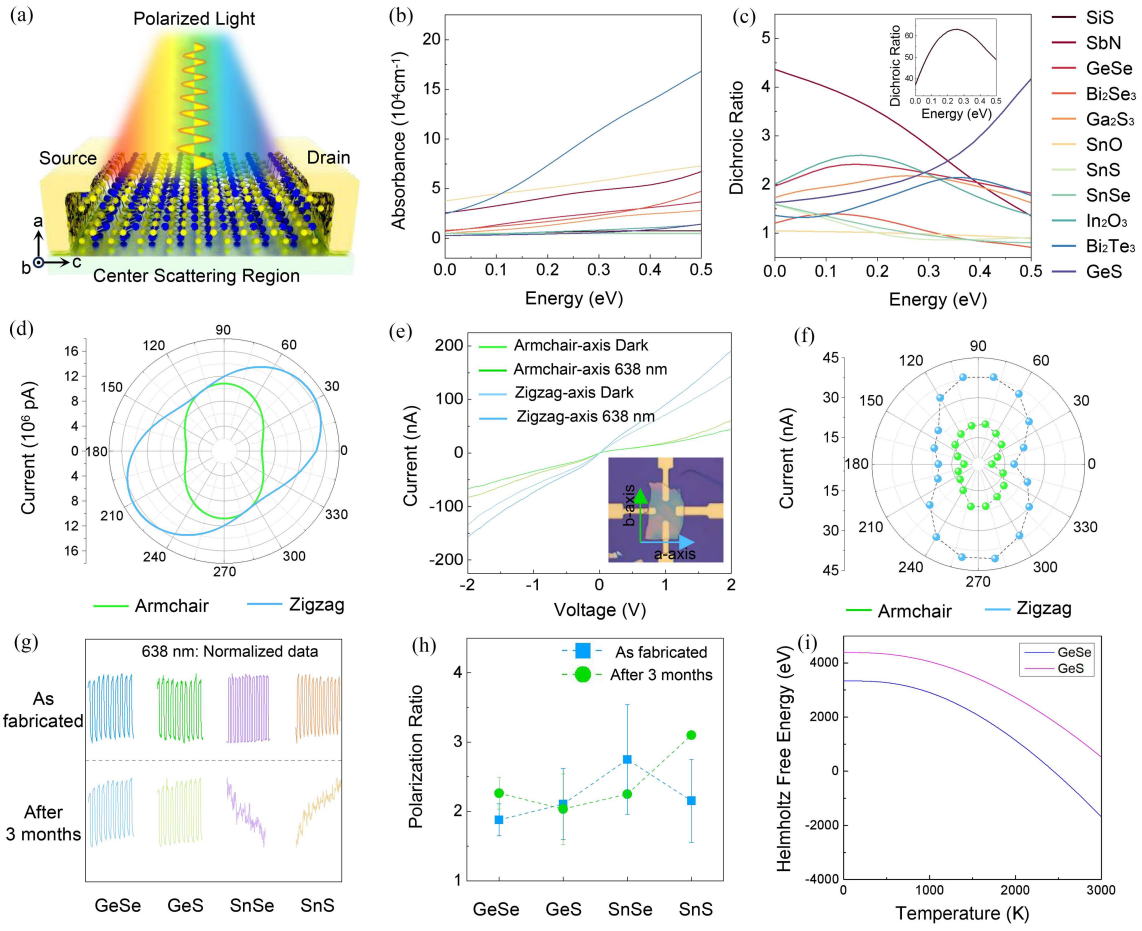

Figure 3 (Color online) (a) Schematic diagram of the model device used to calculate optoelectronic-transport properties for GeSe(S)- and SnSe(S)-based photodetectors. (b) Optical absorbance of monolayer semiconductors with abscissa axis starting with optical band gap. (c) Dichroic ratio of monolayer semiconductors with abscissa axis starting with an optical band gap. (d) Calculated photocurrents are plotted with the linear-polarization laser of 638 nm in the polar coordinates. (e) Output characteristics of GeSe-based photodetector. The inset shows a real image of the typical device based on GeSe with four electrodes constructed in a and b directions. (f) Polarization-sensitive photocurrents are plotted with the linear-polarization laser of 638 nm in the polar coordinates. (g) Time-dependent photocurrent I of the photodetector based on GeSe sample during the light cycling on/off under a positive and negative source-drain voltage V. (h) The statistical values of the polarization ratios (anisotropic current ratios) for five devices in each category (GeSe, GeS, SnSe, and SnS) at 0 days and 3 months after these devices were fabricated. (i) The calculated Helmholtz free energy for 2D GeSe and GeS.

than that along the b-axis, which demonstrates strong anisotropy. The polarization angle-dependent photocurrent was plotted in the polar coordinate system to further characterize the anisotropy of a typical GeSe-based device. Figure 3(f) (Figure S7) clearly illustrates that the polarization dependence of the photocurrent yields two-lobed polar plots, and agrees well with the first-principles calculations (Figure 3(d) and Figure S3). The related values of the polarization ratio (PR) for the GeSe(S)- and SnSe(S)-based devices are listed in Table S1 and are also consistent with the first-principles calculations (Figures 3(b) and (c)). DFT calculations show that GeSe possesses a relatively low Helmholtz free energy and greater stability than GeS (Figure 3(i)). In the experiment, the ambient stability and polarization sensitivity were measured 15 days, 2 months, and 3 months after the devices were fabricated. Figure 3(g) shows the on-off cycling photoresponse characteristics of the GeSe(S)- and SnSe(S)-based devices. After 3 months, a relatively stable photoresponse was shown for the GeSe(S)-based devices, while the SnSe(S)-based devices did not show an evident and stable on/off cycling. This result indicates that GeSe(S)-based devices are more stable than SnSe(S)-based devices. To characterize the polarization sensitivity of these devices, the PR values were measured and are presented in Figure 3(h). Statistical analysis was further conducted on four types of devices. For each category, 5 different devices were measured, and the statistical PR values were compared between the prepared device and the device after 3 months. After the three-month period, only 1 out of 5 devices in both SnSe(S) categories remained viable for the reliable

polarization ratio test, while the other devices failed to produce consistent results. In contrast, all the GeSe(S)-based devices worked normally after three months. By comparing the fluctuation magnitudes of the numerical PR values for GeSe and GeS and considering the smaller individual variations among the five GeSe-based devices (Figure S8), the GeSe-based devices exhibit greater ambient stability. Following a comprehensive analysis of the theoretical computations and experimental measurements, a discerning deduction emerges: materials composed of Ge exhibit greater stability in cationic contexts than their Sn counterparts. Similarly, within anionic configurations, compounds incorporating Se demonstrate greater stability than those containing S (as shown in Figures 3(g) and (h)). Moreover, the materials formed from Ge (Se) are expected to have a higher polarization ratio than those formed from Sn (S) (Figure 3(c)).

3.3 Physical origin of optical anisotropy

To understand the physical origin of optical anisotropy in the 2D orthorhombic monolayers, and using IV-VI compounds SiS, SnS, and GeSe as examples, we calculated their band structures, polarization (P_y), renormalized dichroic ratio (RDR) for optical transitions between the valence band maximum (VBM) and conduction band maximum (CBM), and related wavefunction characteristics, as shown in Figure 4. Here, the polarization (P_y) of the transition from the VBM to the CBM along the K-point path is calculated by the following:

$$P_y = \left|\langle \mu_{\mathrm{CBM}} | \nabla_y | \mu_{\mathrm{VBM}} \rangle\right|^2 / \left|\langle \mu_{\mathrm{CBM}} | \nabla_y | \mu_{\mathrm{VBM}} \rangle\right|^2 + \left|\langle \mu_{\mathrm{CBM}} | \nabla_x | \mu_{\mathrm{VBM}} \rangle\right|^2, \tag{3}$$

where the $\mu_{\mathrm{VBM/CBM}}$, ∇_x, and ∇_y are the wavefunctions of the CBM (VBM) and the derivation operators for x and y, respectively. The polarizations for SnS, GeSe, SiS, SnS/SiS, and SnS/GeSe were calculated, as shown in Figure 4(b). For the monolayers (SnS, GeSe, and SiS), the polarization corresponding to the minimal direct-gap transition completely reaches 1/0, which indicates strong linear dichroism. The polarization can be mapped to the energy bands along the K points in the Brillouin zone (BZ) to further track the possible transition points with large optical anisotropy. SiS has a large energy range (1.24–1.91 eV), and the space between these two arrows in Figure 4(a) is marked in the energy bands; here, complete polarization can be sustained along the y direction. For higher energy transitions, the polarization along the x direction may be obtained at a special energy; however, it may be strongly impacted due to the lower transition occurring for larger photon energies. Thus, SiS can be a good intrinsic y-polarization material. SnS can be x-polarized at the transition near the direct-gap minimum (2.38 eV). With increasing photon energy, the x-polarization is greatly weakened, possibly due to the involvement of some y-polarized transitions. GeSe is completely x-polarized near the direct-gap minimum (1.54 eV), and the x-polarization can be effectively sustained within the energy range (1.54–1.67 eV). To further characterize the polarization absorption with a given photon energy, the RDR can be another good indicator that can establish a connection to the polarization. Here, the RDR is defined as follows:

$$\mathrm{RDR} = \frac{A_y}{A_y + A_x}, \tag{4}$$

where $A_{x/y}$ is the light absorbance along the x (y) directions. The RDRs for SnS, GeSe, SiS, SnS/SiS, and SnS/GeSe were calculated, as shown in Figure 4(c). For these three prototype monolayers, the first peaks all lie near the direct-gap minimum, the corresponding value is close to 1 (0), and similar corresponding polarization trends are observed. The corresponding charge densities (wavefunctions) of the CBM (VBM) at the direct-gap minimum are shown in Figure 4(d). The complete polarization potentially occurred because the mirror symmetry plane was perpendicular to the XY plane, which generally exists in IV-VI compounds with orthorhombic symmetry. As a result, the periodic part of the CBM/VBM Bloch wavefunction ($\mu_{\mathrm{VBM/CBM}}$) has a certain parity along the x or y direction. As depicted in Figure 4(d), the μ_{VBM} and μ_{CBM} of SnS and GeSe have even parity along the x direction. Therefore, the optical transition between the CBM and VBM caused by x-polarized light is symmetrically forbidden because $\langle \mu_{\mathrm{CBM}} | \nabla_x | \mu_{\mathrm{VBM}} \rangle$ (the reduced transition matrix elements for the x direction) is zero, leading to complete y-polarization. For SiS, the μ_{VBM} and μ_{CBM} have even symmetry along the y direction; hence, the corresponding $\langle \mu_{\mathrm{CBM}} | \nabla_y | \mu_{\mathrm{VBM}} \rangle$ (the reduced transition matrix elements for the y direction) is zero. For structures with a monoclinic structure, usually no such mirror plane exists; thus, the $\mu_{\mathrm{VBM/CBM}}$ does not have a particular parity, and the optical anisotropy is smaller than those with an orthorhombic structure. For both SnS/SiS and SnS/GeSe vdW heterostructures, the polarization is close to 1 at their

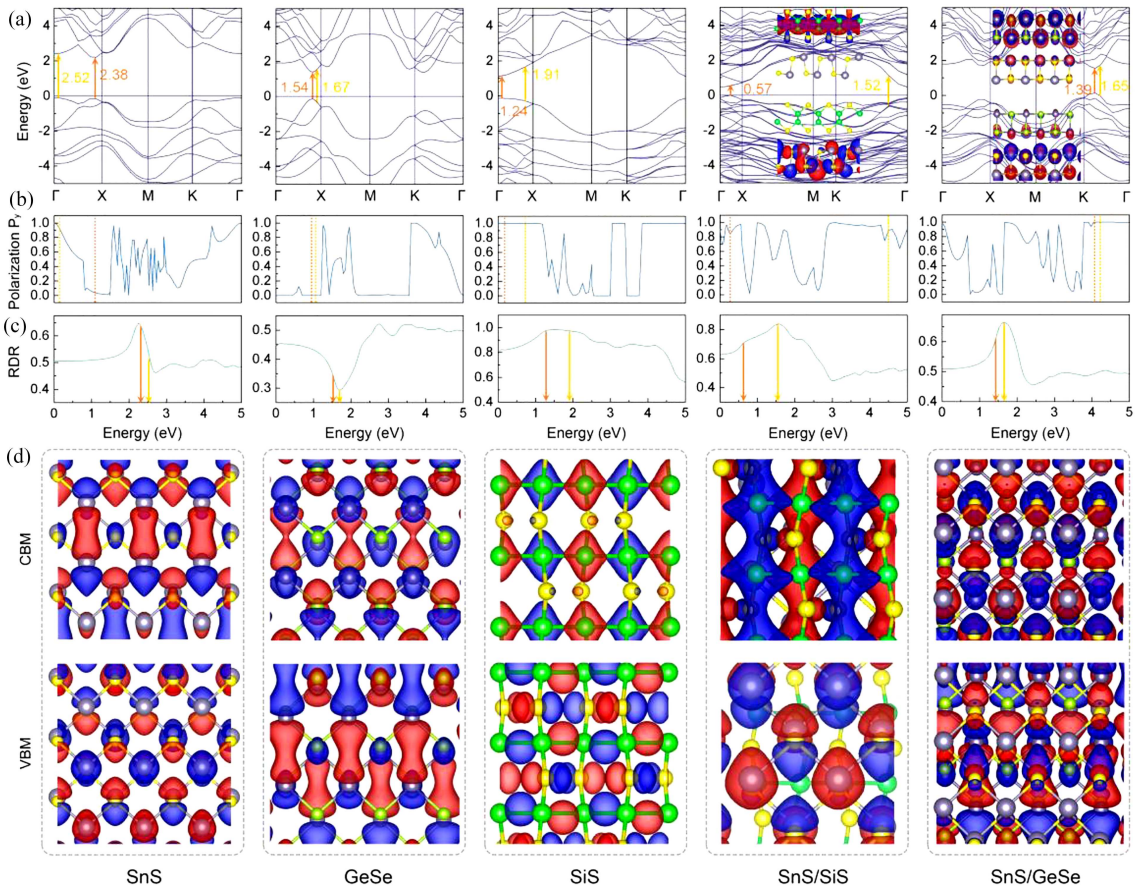

Figure 4 (Color online) (a) Band structures of SnS, GeSe, SiS, SnS/SiS, and SnS/GeSe, respectively. The orange and yellow arrows marked in band structures indicate two critical optical transitions, which correspond to the location of the direct-gap minimum and the peak (valley) energy in the RDR curves. Panels on the energy bands show charge densities at CBM (VBM) of SnS/SiS and SnS/GeSe heterostructures. (b) VBM-to-CBM polarization for SnS, GeSe, SiS, SnS/SiS, and SnS/GeSe, respectively. Dashed lines in the polarization curves correspond to these two critical optical transitions. (c) RDR for SnS, GeSe, SiS, SnS/SiS, and SnS/GeSe, respectively. The arrows mark the RDR at these two transition points. (d) Charge density (wavefunction) distributions at CBM and VBM for SnS, GeSe, SiS, SnS/SiS, and SnS/GeSe, respectively. The wavefunctions of CBM and VBM for single materials and heterostructures are plotted at the K points near the direct-gap minimum.

direct-gap minima (0.57 and 1.39 eV), indicating high y-polarization. This can also be further confirmed by the large value of the corresponding RDR (Figure 4(c)). With higher transition energies (away from the direct-gap minimum), for SnS/SiS (1.52 eV) and SnS/GeSe (1.65 eV), the strongly y-polarized states can be effectively maintained. When the photon energy is further increased, the optical anisotropy is strongly impacted. Therefore, the transition matrix elements of the vdW heterostructure likely exhibit large anisotropy along the X and Y directions, which is due to the certain parity and asymmetry of the wavefunction.

To further study the physical origin of the optical anisotropy of these considered 2D materials, we used the decision tree algorithm to examine the relationship between the LD values and lattice constants as well as the difference in lattice constants, the electronegativity difference between cations and anions, and the periodicity and groups of cations and anions. To use the classification decision tree, we classified materials with an LD value of 0 as No LD, those with an LD value less than 1.5 as Low LD, and those with an LD value greater than or equal to 1.5 as High LD. Seventy-five materials were classified. For the same type of ion, we considered the electronegativity difference to be 0. The programming language we used was Python, and the soft package used was sklearn. Through feature engineering, we found that the classification accuracy is mainly related to the difference in the lattice constants, the difference in electronegativity of the two types of ions, and the point group to which the material belongs. Therefore, we ultimately used these three features for the decision tree classification and achieved a classification accuracy of over 80%. The results from the decision tree classification are shown in Figure 5(a). According to the classification of the first layer of the tree, if the lattice constant difference is less than 0.045 Å,

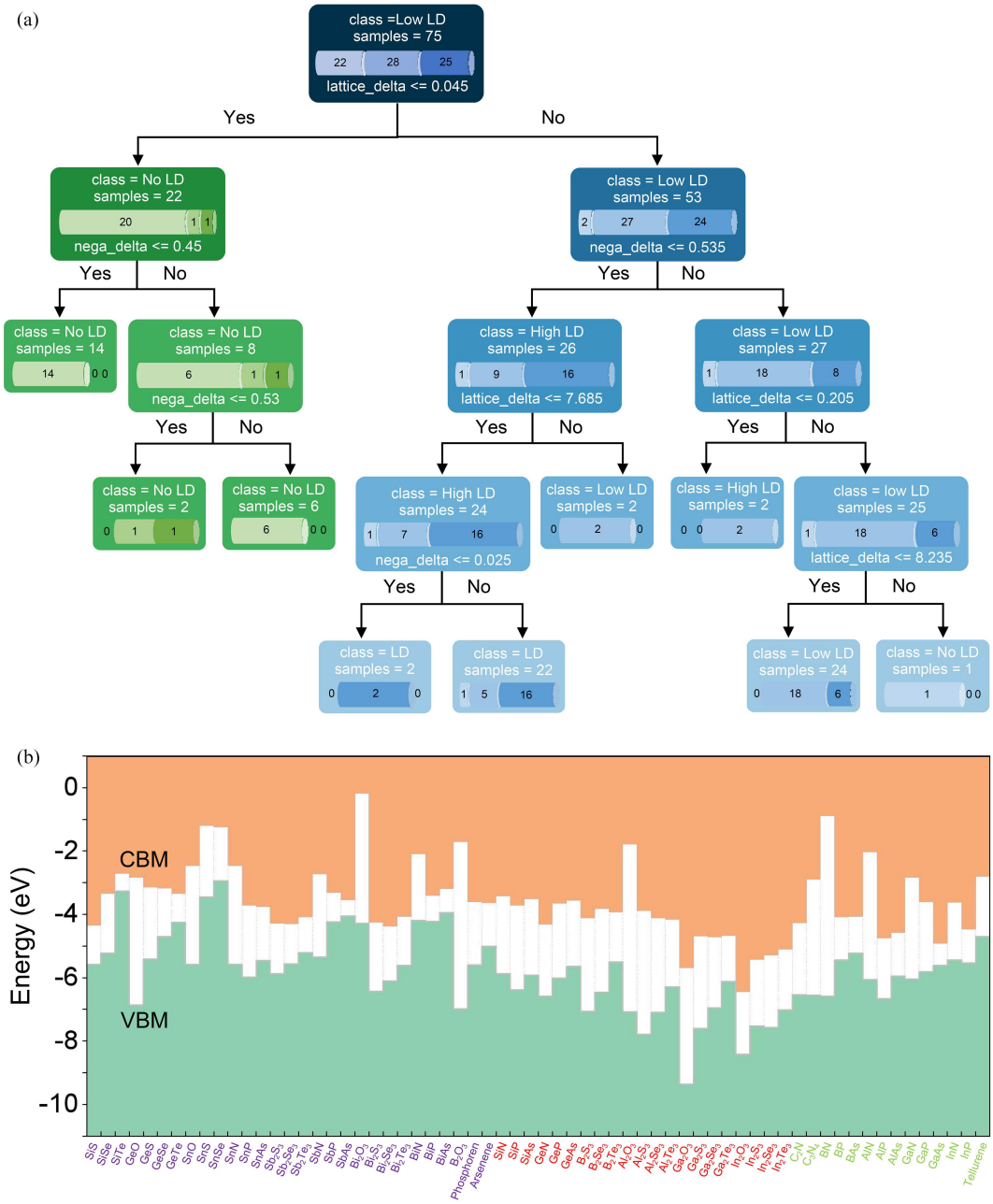

Figure 5 (Color online) (a) Classification decision tree for the relationships among LD, lattice constant, electronegativity, and periodicity of materials generated by using methods. Lattice_delta represents the difference in lattice constants a and b. nega_delta represents the electronegativity difference between two types of ions. Class represents the final classification label obtained in the current node. Samples represent the number of material types included in the current node. Values represent the number of materials belonging to the No LD, Low LD, and High LD groups in the current node. (b) Band alignment of 64 2D semiconductors. The orange and green colors correlate to the conduction band and valence band, respectively. The vacuum space indicates the bandgap of each 2D semiconductor. The vacuum level is selected for the energy reference. The purple, red, and green labels indicate orthorhombic, monoclinic, and hexagonal lattices, respectively.

then the LD of the material is almost always 0. This result provides strong evidence that the difference in the lattice constant determines the LD of two-dimensional materials. The results for the other layers also indicate that the difference in electronegativity of the two types of ions affects the LD of the two-dimensional materials to some extent. A large electronegativity difference can cause an unequal charge distribution between the cations and anions. This results in an asymmetric wavefunction distribution and may induce optical anisotropy. Thus, these results demonstrate that 2D materials with large lattice constant and electronegativity differences incline to show high optical anisotropy.

From the perspective of device applications based on vdW heterostructures, the band offset plays a

crucial role by affecting the carrier transport. Type-I alignment describes the confinement of charge carriers, which is desired in semiconductor lasers, and type-II alignment is beneficial for the spatial separation of electrons and holes and is, thus, widely used in the solar cell industry. Due to the great dislocation of band edges in type-III alignment, these materials could be used for quantum tunneling devices. Using the vacuum potentials as a reference, we calculated the band alignment of all 2D semiconductors. Figure 5(b) shows the original band alignment among all aforementioned 2D semiconductors, where three types of band alignment can be achieved by forming specific heterostructures. Note that the original band alignment may be slightly shifted due to charge transfer when forming vdW heterostructures, and it does not affect the conclusion. Thus, this database can provide large property diversity (such as bandgap, optical anisotropy, the type of band alignment, and their combinations), which facilitates multifunctional and lensless polarization-sensitive optoelectronic devices.

4 Conclusion

In conclusion, in view of the unclear physical origin of linear dichroism and the lack of systematic theoretical summaries and guidance for 2D semiconductors composed of main group elements (groups III, IV, V, and VI), we constructed a database. In our 2D optical dichroism database, first-principles calculations were performed on 100 kinds of 2D materials, including 65 compounds, 10 elementary materials, and 25 vdW heterostructures. In terms of the lattice symmetry, 2D materials can be classified into three groups: orthorhombic, monoclinic, and hexagonal. Notably, the in-plane lattice asymmetry could be the origin of the optical anisotropy because 2D materials with orthorhombic and monoclinic structures tend to have considerable optical linear dichroism, while their hexagonal counterparts are optically isotropic. Specifically, orthorhombic 2D materials possess larger optical anisotropy, and this large anisotropy could be attributed to the intrinsic mirror plane in the lattice and the in-plane parity of the CBM and VBM wavefunctions, which then leads to a completely polarized optical transition. In addition, the formation of vdW heterostructures helps to improve the light absorption of the system and effectively preserves the optical anisotropy of the materials. More importantly, various types of band alignment can be formed, which greatly enriches the application of the 2D materials and heterostructures with in-plane LD.

Acknowledgements This work was supported by National Natural Science Foundation of China (Grant Nos. 62125404, 12074029, 11991060, 12393831), Beijing Natural Science Foundation (Grant No. Z220005), Strategic Priority Research Program of Chinese Academy of Sciences (Grant No. XDB43000000), and CAS Project for Young Scientists in Basic Research (Grant No. YSBR-026).

Supporting information Figures S1–S8 and Table S1. The supporting information is available online at info.scichina.com and link.springer.com. The supporting materials are published as submitted, without typesetting or editing. The responsibility for scientific accuracy and content remains entirely with the authors.

References

1 Xu H, Niu J R, Chen P, et al. A fast radio burst source at a complex magnetized site in a barred galaxy. Nature, 2022, 609: 685–688
2 Biswas S, Grajower M Y, Watanabe K, et al. Broadband electro-optic polarization conversion with atomically thin black phosphorus. Science, 2021, 374: 448–453
3 Wei J, Chen Y, Li Y, et al. Geometric filterless photodetectors for mid-infrared spin light. Nat Photon, 2023, 17: 171–178
4 Hu H, Chen N, Teng H, et al. Gate-tunable negative refraction of mid-infrared polaritons. Science, 2023, 379: 558–561
5 Kim S E, Mujid F, Rai A, et al. Extremely anisotropic van der Waals thermal conductors. Nature, 2021, 597: 660–665
6 Rodger A, Nordén B. Circular Dichroism and Linear Dichroism. Oxford: Oxford University Press, 1997
7 Nordén B. Applications of linear dichroism spectroscopy. Appl Spectr Rev, 1978, 14: 157–248
8 Pei J, Gai X, Yang J, et al. Producing air-stable monolayers of phosphorene and their defect engineering. Nat Commun, 2016, 7: 10450
9 Li P, Zhang D, Liu J, et al. Air-stable black phosphorus devices for ion sensing. ACS Appl Mater Interfaces, 2015, 7: 24396–24402
10 He J, He D, Wang Y, et al. Exceptional and anisotropic transport properties of photocarriers in black phosphorus. ACS Nano, 2015, 9: 6436–6442
11 Feng J, Yan X, Liu Y, et al. Crystallographically aligned perovskite structures for high-performance polarization-sensitive photodetectors. Adv Mater, 2017, 29: 1605993
12 Zhang E, Wang P, Li Z, et al. Tunable ambipolar polarization-sensitive photodetectors based on high-anisotropy $ReSe_2$ nanosheets. ACS Nano, 2016, 10: 8067–8077
13 Yuan H, Liu X, Afshinmanesh F, et al. Polarization-sensitive broadband photodetector using a black phosphorus vertical p-n junction. Nat Nanotech, 2015, 10: 707–713
14 Chai R, Chen Y, Zhong M, et al. Non-layered ZnSb nanoplates for room temperature infrared polarized photodetectors. J Mater Chem C, 2020, 8: 6388–6395
15 Wang J, Jiang C, Li W, et al. Anisotropic low-dimensional materials for polarization-sensitive photodetectors: from materials to devices. Adv Opt Mater, 2022, 10: 2102436

16 Wang T, Zhao K, Wang P, et al. Intrinsic linear dichroism of organic single crystals toward high-performance polarization-sensitive photodetectors. Adv Mater, 2022, 34: 2105665
17 Tyo J S, Goldstein D L, Chenault D B, et al. Review of passive imaging polarimetry for remote sensing applications. Appl Opt, 2006, 45: 5453–5469
18 Laux E, Genet C, Skauli T, et al. Plasmonic photon sorters for spectral and polarimetric imaging. Nat Photon, 2008, 2: 161–164
19 Nayar S K, Fang X S, Boult T. Separation of reflection components using color and polarization. Int J Comput Vision, 1997, 21: 163–186
20 Wang X, Li Y, Huang L, et al. Short-wave near-infrared linear dichroism of two-dimensional germanium selenide. J Am Chem Soc, 2017, 139: 14976–14982
21 Wang Z H, Xu B, Pei S H, et al. Recent progress in 2D van der Waals heterostructures: fabrication, properties, and applications. Sci China Inf Sci, 2022, 65: 211401
22 Ning H K, Yu Z H, Li T T, et al. From lab to fab: path forward for 2D material electronics. Sci China Inf Sci, 2023, 66: 160411
23 Shen W, Hu C, Huo S, et al. Wavelength tunable polarizer based on layered black phosphorus on Si/SiO_2 substrate. Opt Lett, 2018, 43: 1255–1258
24 Wang X, Zhong F, Kang J, et al. Polarizer-free polarimetric image sensor through anisotropic two-dimensional GeSe. Sci China Mater, 2021, 64: 1230–1237
25 Zhou F, Zhang J. Polarization-independent black-phosphorus polarizer in visible regime. IEEE Photon Technol Lett, 2017, 29: 1923–1926
26 Zheng Z P, Huang Y J, Wu F, et al. Multidimensional modulation of light fields via a combination of two-dimensional materials and meta-structures. Sci China Inf Sci, 2023, 66: 160403
27 Li X, Liu H, Ke C, et al. Review of anisotropic 2D materials: controlled growth, optical anisotropy modulation, and photonic applications. Laser & Photon Rev, 2021, 15: 2100322
28 Xiao M, Yang H, Shen W, et al. Symmetry-reduction enhanced polarization-sensitive photodetection in core-shell SbI_3/Sb_2O_3 van der Waals heterostructure. Small, 2020, 16: 1907172
29 Gambardella P, Rusponi S, Veronese M, et al. Giant magnetic anisotropy of single cobalt atoms and nanoparticles. Science, 2003, 300: 1130–1133
30 Hafeez M, Gan L, Li H, et al. Chemical Vapor deposition synthesis of ultrathin hexagonal $ReSe_2$ flakes for anisotropic Raman property and optoelectronic application. Adv Mater, 2016, 28: 8296–8301
31 Geim A K, Novoselov K S. The rise of graphene. Nat Mater, 2007, 6: 183–191
32 Ganatra R, Zhang Q. Few-layer MoS_2: a promising layered semiconductor. ACS Nano, 2014, 8: 4074–4099
33 Tran V, Soklaski R, Liang Y, et al. Layer-controlled band gap and anisotropic excitons in few-layer black phosphorus. Phys Rev B, 2014, 89: 235319
34 Silva-Guillén J A, Canadell E, Guinea F, et al. Strain tuning of the anisotropy in the optoelectronic properties of TiS_3. ACS Photonics, 2018, 5: 3231–3237
35 Wolverson D, Crampin S, Kazemi A S, et al. Raman spectra of monolayer, few-layer, and bulk $ReSe_2$: an anisotropic layered semiconductor. ACS Nano, 2014, 8: 11154–11164
36 Pi L, Hu C, Shen W, et al. Highly in-plane anisotropic 2D $PdSe_2$ for polarized photodetection with orientation selectivity. Adv Funct Mater, 2021, 31: 2006774
37 Zhou X, Zhang Q, Gan L, et al. Booming development of group IV-VI semiconductors: fresh blood of 2D family. Adv Sci, 2016, 3: 1600177
38 Yao J, Zheng Z, Yang G. All-layered 2D optoelectronics: a high-performance UV-vis-NIR broadband SnSe photodetector with Bi_2Te_3 topological insulator electrodes. Adv Funct Mater, 2017, 27: 1701823
39 Simon J, Protasenko V, Lian C, et al. Polarization-induced hole doping in wide-band-gap uniaxial semiconductor heterostructures. Science, 2010, 327: 60–64
40 Zhang J, Dong P, Dang K, et al. Ultra-wide bandgap semiconductor Ga_2O_3 power diodes. Nat Commun, 2022, 13: 3900
41 Kresse G, Furthmüller J. Efficient iterative schemes for ab initio total-energy calculations using a plane-wave basis set. Phys Rev B, 1996, 54: 11169–11186
42 Perdew J P, Burke K, Ernzerhof M. Generalized gradient approximation made simple. Phys Rev Lett, 1996, 77: 3865–3868
43 Heyd J, Peralta J E, Scuseria G E, et al. Energy band gaps and lattice parameters evaluated with the Heyd-Scuseria-Ernzerhof screened hybrid functional. J Chem Phys, 2005, 123: 174101
44 Grimme S, Antony J, Ehrlich S, et al. A consistent and accurate ab initio parametrization of density functional dispersion correction (DFT-D) for the 94 elements H-Pu. J Chem Phys, 2010, 132: 154104
45 Brandbyge M, Mozos J L, Ordejón P, et al. Density-functional method for nonequilibrium electron transport. Phys Rev B, 2002, 65: 165401
46 Henrickson L E. Nonequilibrium photocurrent modeling in resonant tunneling photodetectors. J Appl Phys, 2002, 91: 6273–6281
47 Smidstrup S, Markussen T, Vancraeyveld P, et al. QuantumATK: an integrated platform of electronic and atomic-scale modelling tools. J Phys-Condens Matter, 2019, 32: 015901
48 Chen J, Hu Y, Guo H. First-principles analysis of photocurrent in graphene PN junctions. Phys Rev B, 2012, 85: 155441
49 Gao Q, Kang J, Wei Z, The 2D optical LD database. https://github.com/qGAO12345/qGAO12345/blob/main/2D%20optical%20materials.zip
50 Zhou Z, Shen T, Wang P, et al. Low symmetric sub-wavelength array enhanced lensless polarization-sensitivity photodetector of germanium selenium. Sci Bull, 2023, 68: 173–179
51 Zhong M, Meng H, Liu S, et al. In-plane optical and electrical anisotropy of 2D black arsenic. ACS Nano, 2021, 15: 1701–1709
52 Gao Q, Li X, Fang L, et al. Exciton states and oscillator strength in few-layer α-tellurene. Appl Phys Lett, 2019, 114: 092101
53 Zhu Z, Cai X, Yi S, et al. Multivalency-driven formation of te-based monolayer materials: a combined first-principles and experimental study. Phys Rev Lett, 2017, 119: 106101
54 Late D J, Liu B, Matte H S S R, et al. Rapid characterization of ultrathin layers of chalcogenides on SiO_2/Si substrates. Adv Funct Mater, 2012, 22: 1894–1905
55 Xu M, Liang T, Shi M, et al. Graphene-like two-dimensional materials. Chem Rev, 2013, 113: 3766–3798
56 Wang Z, Safdar M, Mirza M, et al. High-performance flexible photodetectors based on GaTe nanosheets. Nanoscale, 2015, 7: 7252–7258